

ABSTRACT

Title of dissertation: Measuring topology of BECs
in a synthetic dimensions lattice

Dina Genkina
Doctor of Philosophy, 2018

Dissertation directed by: Professor Ian Spielman
Department of Physics

Measuring topology of BECs in a synthetic dimensions lattice

by

Dina Genkina

Dissertation submitted to the Faculty of the Graduate School of the
University of Maryland, College Park in partial fulfillment
of the requirements for the degree of
Doctor of Philosophy
2018

Advisory Committee:
Professor Ian Spielman, Chair/Advisor

© Copyright by
Dina Genkina
2018

Table of Contents

List of Tables	6
List of Figures	7
2 Introduction	1
2.1 Bose-Einstein condensation	1
2.1.1 Phase transition of a non-interacting Bose gas	1
2.1.2 Interacting Bose gas	6
2.2 Degenerate Fermi Gas	10
2.2.1 Fermi statistics and the onset of degeneracy	10
2.2.2 Interactions and Feshbach resonances	12
2.3 RbK apparatus	15
2.3.1 Laser beams	17
2.3.2 Magnetic coils	19
2.3.3 Procedure for making a BEC	21
2.3.4 Changes to apparatus for Rubidium	26
2.3.4.1 Master laser setup	26
2.3.4.2 Alignment imaging path	26
2.3.4.3 ODT beam shaping	26
2.3.5 Procedure for making a DFG	26
2.3.6 Current status of Potassium apparatus	30
Bibliography	36

List of Tables

List of Figures

1	Occupation of energy states of a 3-D harmonic oscillator. The trapping frequencies are $\omega_x = \omega_y = \omega_z = 2\pi 50$ Hz, and the atom number is $N = 10^6$. Dots represent the total fractional population in 50 adjacent energy levels, including degeneracies. The stars represent the fractional population in just the ground state.	4
2	Time-of-flight images of atoms. (a) Above the critical temperature - the atoms are thermally distributed. (b) Below the critical temperature - about half of the atoms are condensed in the central peak. (c) Far below the critical temperature - almost all atoms are condensed in the central peak.	5
3	In situ measurement of a fraction of bose condensed atoms. (a) Absorption image taken of $\approx 1\%$ of the cloud. The x and y axes represent x and y position, while color represents the atom number. (b) The blue line repesents atom number as a function of position along hte x axis, integrated over the y axis. The black dashed line represents the best fit of a Gaussian function to the atomic distribution. The dashed red line represents the best fit of a Thomas-Fermi profile to the atomic distribution.	9
4	Occupation number as a function of energy for a Fermi gas of $N = 10^6$ atoms in a 3-D harmonic oscillator with frequencies $\omega_x = \omega_y = \omega_z = 2\pi 50$ Hz. The Fermi temperature for these parameters is $T_F = 436$ nK.	12
5	Schematic of a Feshbach resonance. (a) Pictoral representation of energy as a function of interatomic distance for an open channel (red) and closed channel (blue). (b) Energy as a function of background magnetic field B for the closed (blue) and open (red) channels. The energies coincide at the Feshbach resonance point B_0 . Energy of Figure taken from [1].	14
6	Photograph of RbK apparatus at NIST Gaithersburg. The main science chamber is at the center, hidden behind optics and coils. The Zeeman slower connects the atomic ovens (not shown) to the chamber. There are several levels of breadboards on which optics are mounted, labelled here as basement (surface of optical table), main floor, balcony and attic.	16

7	Schematic of RbK apparatus. (a) Side view of apparatus. Only beams propagating along the e_z direction through the atoms are pictured. (b) Top view of apparatus. Only beams propagating along the x - y plane are shown. Schematic is not to scale and the angles are approximate.	18
8	Schematic of magnetic coils on the RbK apparatus. The black wire frame represents the main experiment chamber, with the Zeeman slower off to the right. The Zeeman slower and reverse coils are wound around the Zeeman slower in varying spatial frequency (magenta). The quad (orange), gradient cancellation dB_z/dz (bright green) and biasZ (brown) are all pairs of identical coils on the top and bottom of the apparatus. Bias X-Y coils (red) are a pair of identical coils around the axes of the M_1 and M_3 mirrors, and the bias X+Y (dark green) are a pair of identical coils around the axes of the M_2 and M_4 mirrors. The rf coils (blue) are a pair of circular coils on top of the experimental chamber, spaced enough to allow the top MOT beam through. The gradient cancellation coils dB_{x+y}/dz (cyan) are four square coils on top and bottom of the experiment along the X+Y axis.	20
9	24
10	24
11	25
12	27
13	28
14	Schematic of the 2D MOT setup. The mini-conflat on the right is to be attached to the existing experiment chamber, directing the atomic beam into the 3D MOT.	32
15	Picture of 2D MOT cell during an attempt to epoxy AR coated windows onto the stainless steel frame. The clamps serve to hold the windows in place while epoxy cures.	33
16	Schematic of 2D MOT optics along one direction. the main cooling and repump beam is split into four parallel arms by four beam splitter cubes. The push beam enters from the oven direction and is retro-reflected via a custom machined and polished differential pumping tube. These optics are mounted on crosses attached to the 2D MOT cell.	34
17	Picture of current 2D MOT apparatus. The vacuum system is in place, optics are (mostly) mounted and coils to generate the quadrupole trap and cancel gradients along the atomic beam direction have been wound.	35

Chapter 2: Introduction

2.1 Bose-Einstein condensation

2.1.1 Phase transition of a non-interacting Bose gas

Bose gases are characterized by the Bose-Einstein distribution giving the number of atoms $n(E_j)$ occupying each energy eigenstate E_j as

$$n(E_j) = \frac{1}{e^{(E_j - \mu)/k_B T} - 1}, \quad (2.1)$$

where k_B is the Boltzmann constant, T is the temperature in Kelvin, μ is the chemical potential. Assuming the total atom number N is fixed, the chemical potential $\mu(T, N)$ ensures that the total occupation of all $\sum_j n(E_j) = N$.

The Bose distribution leads to Bose-Einstein condensation, the collapse of a macroscopic fraction of the atoms into the ground state. This comes as a direct consequence of the Bose distribution's characteristic -1 in the denominator. Consider the occupation number $n(E_j)$ —it must remain positive, as a negative occupation number is unphysical. That means that the quantity $e^{(E_j - \mu)/k_B T}$ must remain greater than 1, or $(E_j - \mu)/k_B T < 0$ for all E_j . Therefore, $\mu \leq E_0$, where E_0 is the ground state energy.

Then, for a given temperature T , there is a maximum occupation number for each excited state given by $n(E_j) = \frac{1}{e^{E_j/k_B T} - 1}$. The only energy state whose occupation number is unbounded is the ground state, as $n(E_0)$ tends toward infinity as μ

tends towards 0. Therefore, as the temperature decreases, the maximum occupation of each excited state decreases until they can no longer support all of the atoms. The remaining atoms then have no choice but to collapse into the lowest energy level and Bose condense.

We will show this quantitatively for the case of a 3-D harmonically trapped gas of atoms, relevant to the experiments described in this thesis. It is convenient to define the fugacity $\zeta = e^{\mu/k_B T}$, and re-write the Bose-Einstein distribution as eigenstate E_j as

$$n(E_j) = \frac{\zeta}{e^{E_j/k_B T} - \zeta}. \quad (2.2)$$

The harmonic oscillator potential can be written as

$$V(r) = \frac{1}{2}m(\omega_x^2x^2 + \omega_y^2y^2 + \omega_z^2z^2), \quad (2.3)$$

where ω_x , ω_y and ω_z are the angular trapping frequencies along \mathbf{e}_x , \mathbf{e}_y , and \mathbf{e}_z . The eigenenergies with this potential are

$$E(j_x, j_y, j_z) = \left(\frac{1}{2} + j_x\right)\hbar\omega_x + \left(\frac{1}{2} + j_y\right)\hbar\omega_y + \left(\frac{1}{2} + j_z\right)\hbar\omega_z. \quad (2.4)$$

In order to find μ , we must find $\sum_{j_x, j_y, j_z} n(E(j_x, j_y, j_z))$ and set it equal to N . This task is greatly simplified by going to the continuum limit and finding the density of states. To do this, we neglect the zero-point energy (setting $E_0 = 0$, the effects of the zero-point energy are discussed in [?] section 2.5) and assume there is on average one state per volume element $\hbar^3\omega_x\omega_y\omega_z$. Then, the total number of states with energy less than or equal to some value ϵ is given by the volume of a prism made between points $(x, y, z) = (0, 0, 0), (\epsilon, 0, 0), (0, \epsilon, 0)$ and $(0, 0, \epsilon)$ in units of the volume element:

$$G(\epsilon) = \frac{\epsilon^3}{6\hbar^3\omega_x\omega_y\omega_z}. \quad (2.5)$$

The density of states is given by

$$g(\epsilon) = \frac{d}{d\epsilon}G(\epsilon) = \frac{\epsilon^2}{3\hbar^3\omega_x\omega_y\omega_z}. \quad (2.6)$$

Note that the occupation of the ground state is not included in this continuum picture. We can therefore use it only to calculate the total number of atoms in all of the excited states:

$$N_{\text{ex}} = \int_0^\infty d\epsilon g(\epsilon)n(\epsilon) = \int_0^\infty d\epsilon \frac{\epsilon^2}{3\hbar\omega_x\omega_y\omega_z} \frac{\zeta}{e^{\epsilon/k_B T} - \zeta} = \frac{(k_B T)^3}{\hbar^3\omega_x\omega_y\omega_z} \text{Li}_3(\zeta), \quad (2.7)$$

where $\text{Li}_3(\zeta)$ is the polylogarithm function¹. We define the mean trapping frequency $\bar{\omega} = (\omega_x\omega_y\omega_z)^{1/3}$ and the harmonic oscillator energy as $\hbar\bar{\omega}$, with the thermal energy in harmonic oscillator units $\tau = k_B T/\hbar\bar{\omega}$, giving

$$N_{\text{ex}} = \tau^3 \text{Li}_3(\zeta). \quad (2.8)$$

Finding the occupation number of the ground state from the Bose-Einstein distribution

$$N_0 = \frac{\zeta}{1 - \zeta}, \quad (2.9)$$

we can then find the chemical potential, or equivalently the fugacity ζ , to satisfy

$$N = N_0 + N_{\text{ex}}. \quad (2.10)$$

This is a transcendental equation that can only be solved numerically. We present an example of the solution in Figure 1. Here, we have calculated the fractional population in different harmonic oscillator energy levels for three different temperatures, using trapping frequencies are $\omega_x = \omega_y = \omega_z = 2\pi 50$ Hz, and atom number $N = 10^6$.

¹This calculation was done with Wolfram Alpha, not Russian algebra skills

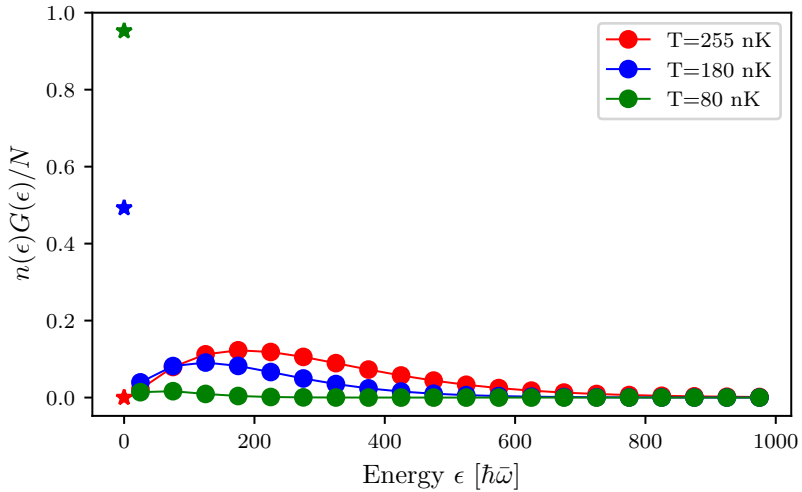


Figure 1: Occupation of energy states of a 3-D harmonic oscillator. The trapping frequencies are $\omega_x = \omega_y = \omega_z = 2\pi 50$ Hz, and the atom number is $N = 10^6$. Dots represent the total fractional population in 50 adjacent energy levels, including degeneracies. The stars represent the fractional population in just the ground state.

For energies above the ground state (dots in the figure), we binned 50 energy levels together, such that each dot represents the total fractional population in 50 adjacent levels. This was obtained by integrating eqn. 2.7 from $\epsilon - 25\hbar\bar{\omega}$ to $\epsilon + 25\hbar\bar{\omega}$. The stars represent the fractional population in just the ground state, calculated from eqn. 2.9. Note that at temperature $T = 255$ nK (red), the ground state population is consistent with a continuous extrapolation from the excited state populations and is almost zero. At lower temperatures, $T = 180$ nK (blue) the ground state population is in excess of any reasonable extrapolation from the excited state fractions, and at $T = 80$ nK (green) almost all the atoms are in the ground state.

The onset of Bose-Einstein condensation occurs at a critical temperature T_c . This temperature is defined as the temperature at which the occupation number of excited states is equal to the atom number, ie when the atoms have occupied all available excited states and any remaining atoms will have to pile into the ground state. Since the maximal occupation of the excited states will occur at $\mu = 0$,

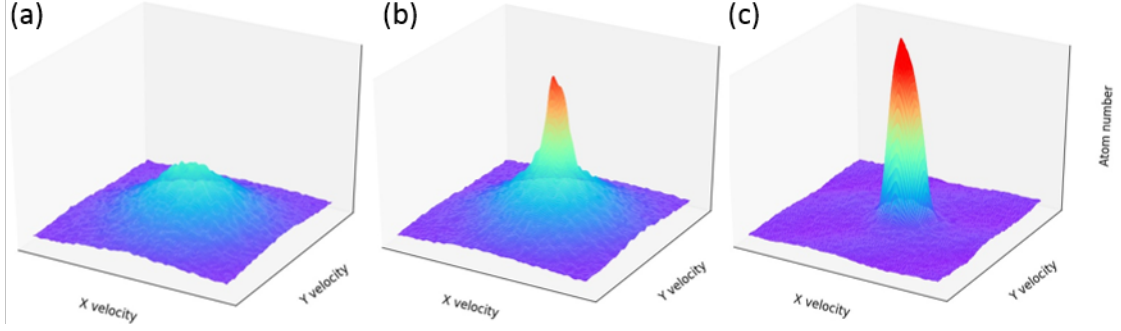


Figure 2: Time-of-flight images of atoms. (a) Above the critical temperature - the atoms are thermally distributed. (b) Below the critical temperature - about half of the atoms are condensed in the central peak. (c) Far below the critical temperature - almost all atoms are condensed in the central peak.

the occupation of the excited state is bounded from above by $N_{\text{ex}}(\mu = 0)$, and the critical temperature is defined by

$$N = N_{\text{ex}}(\mu = 0, T = T_c) = \frac{(k_B T_c)^3}{\hbar^3 \omega_x \omega_y \omega_z} Li_3(\zeta = 1). \quad (2.11)$$

Using $Li_3(1) \approx 1.202$, we obtain for a given atom number and trapping frequencies

$$T_c = \frac{1.202 N}{k_B^3} \hbar^3 \omega_x \omega_y \omega_z. \quad (2.12)$$

For the parameters in Figure 1, $T_c = 225$ nK.

For temperatures below the critical temperature, the condensation fraction f_c —the fraction of atoms in the ground state—is directly related to the ratio of the temperature to the critical temperature:

$$f_c = 1 - \frac{N}{N_{\text{ex}}} = 1 - \frac{(k_B T)^3}{\hbar^3 \omega_x \omega_y \omega_z} Li_3(\zeta = 1) = 1 - \left(\frac{T}{T_c} \right)^3, \quad (2.13)$$

where in the last step we have plugged in the definition of the critical temperature eqn. 2.12.

Figure 2 shows the progression towards condensation as the temperature of

a cloud of ^{87}Rb is decreased below T_c . The images are obtained via a time-of-flight measurement (see section ??), where the atoms are allowed to expand freely, mapping the initial momentum to final position, imaged via absorption imaging (see section ??). The x and y axes represent momentum along x and y , while the z axis represents the number of atoms. The z axis momentum is integrated over. Figure 2a shows a cloud above the condensation temperature - the momentum distribution is gaussian, given by the Maxwell-Boltzmann distribution. In fig. 2b, the temperature has been decreased below T_c , and about half the atoms have collapsed into the ground state, producing a large peak in atom number around zero momentum. In fig. 2c, the temperature has been decreased even further and almost all the atoms populate the central peak - the distribution is no longer gaussian but a sharp peak around zero momentum.

2.1.2 Interacting Bose gas

In the previous section, we assumed there was no interaction between the atoms other than that enforced by statistics. In this section, we will relax this assumption somewhat and describe the condensed atomic state through its characteristic Gross-Pitaevskii equation.

Since condensation occurs at very low temperatures, and thus very low kinetic energies, we can assume that any scattering processes between the atoms are s -wave and can be described simply by a scattering length a . For ^{87}Rb , relevant to experiments described in this thesis, the scattering length between two atoms in the $F = 2$ hyperfine state is $a = 95.44(7)a_0$ [?], where $a_0 = 5.29 \times 10^{-11}$ m is the Bohr radius. The short-range interaction between two particles can be approximated as a contact interaction with an effective strength U_0 as (see [?] section 5.2.1):

$$U(r_1, r_2) = U_0\delta(r_1 - r_2) = \frac{4\pi\hbar^2 a}{m}\delta(r_1 - r_2), \quad (2.14)$$

where m is the atomic mass and δ is the Dirac delta function. The full Hamiltonian of the many-body system is then

$$H = \sum_i \frac{p_i^2}{2m} + V(r_i) + U_0 \sum_{i < j} \delta r_i - r_j, \quad (2.15)$$

where i labels the particles, p_i is the momentum, r_i is the position, and V is the external potential.

We make the mean field approximation by assuming that no interactions between two atoms take them out of the ground state, and hence all atoms can be assumed to be in the same single particle wavefunction, making the overall wavefunction

$$\Psi(r_1, r_2, \dots, r_N) = \prod_i \phi(r_i), \quad (2.16)$$

where ϕ is the single particle wavefunction. It is convenient to define the wavefunction of the condensed state, $\psi(r) = \sqrt{N}\phi(r)$, making the normalization $N = \int dr |\psi(r)|^2$.

The energy of this wavefunction under the Hamiltonian above is given by

$$E = \int dr \left[\frac{\hbar^2}{2m} |\nabla \psi(r)|^2 + V(r) |\psi(r)|^2 + \frac{1}{2} U_0 |\psi(r)|^4 \right] \quad (2.17)$$

Given N particles, there are $N(N - 1)/2$ unique pairs of particles that can have a pairwise interaction, approximately equal to $N^2/2$ for large N . The N^2 is absorbed into the definition of ψ , but the factor of $1/2$ remains on the final interaction term. The task of finding the condensed eigenstate reduces to minimizing this energy under the normalization constraint $N = \int dr |\psi(r)|^2$. This can be done by using the method of Lagrange multipliers to minimize $E - \mu N$. Then, we can minimize this quantity by finding the point where the derivative with respect to ψ and ψ^* is zero.

Taking the derivative with respect to ψ^* we obtain

$$-\frac{\hbar^2}{2m} \nabla^2 \psi(r) + V(r)\psi(r) + U_0|\psi(r)|^2\psi(r) = \mu\psi(r), \quad (2.18)$$

which is the Gross-Pitaevskii equation. This is a non-linear equation that generally needs to be solved numerically.

There is another approximation that can be made in cases where the atomic density is high enough that the interaction energy is significantly larger than the kinetic energy. Then, the kinetic term in the Hamiltonian can be neglected. This is called the Thomas-Fermi approximation. Then, the wavefunction is given simply by

$$|\psi(r)|^2 = \frac{\mu - V(r)}{U_0}. \quad (2.19)$$

In this approximation, the probability density simply takes the form of the inverse of the potential. In the case of a harmonically trapped BEC, it is shaped like an inverted parabola. The Thomas-Fermi radius, ie the extent of the particle wavefunction, is the point where the probability density goes to zero: $\mu - V(r_0) = 0$. For a harmonic trap, along any direction, this is given by $r_0^2 = 2\mu/m\omega^2$.

Figure 3a shows an absorption image of a small fraction of a BEC in situ (see section ??), meaning as they are in the trap - without expanding in time-of-flight. Therefore, the x and y axis represent position, while color represents the atom number. Figure 3b shows the atom number integrated over the y-axis in blue. The red dashed lines represent a best fit line to a Thomas-Fermi distribution, here an inverse parabola. The black dashed lines represent a best fit of a Gaussian to the atomic distribution. The Thomas-Fermi distribution matches the atomic distribution more closely in the center where the density is high, but the Gaussian distribution does a better job at the tails of the distribution. This is due to the presence of some thermal atoms, which remain Maxwell-Boltzmann distributed.

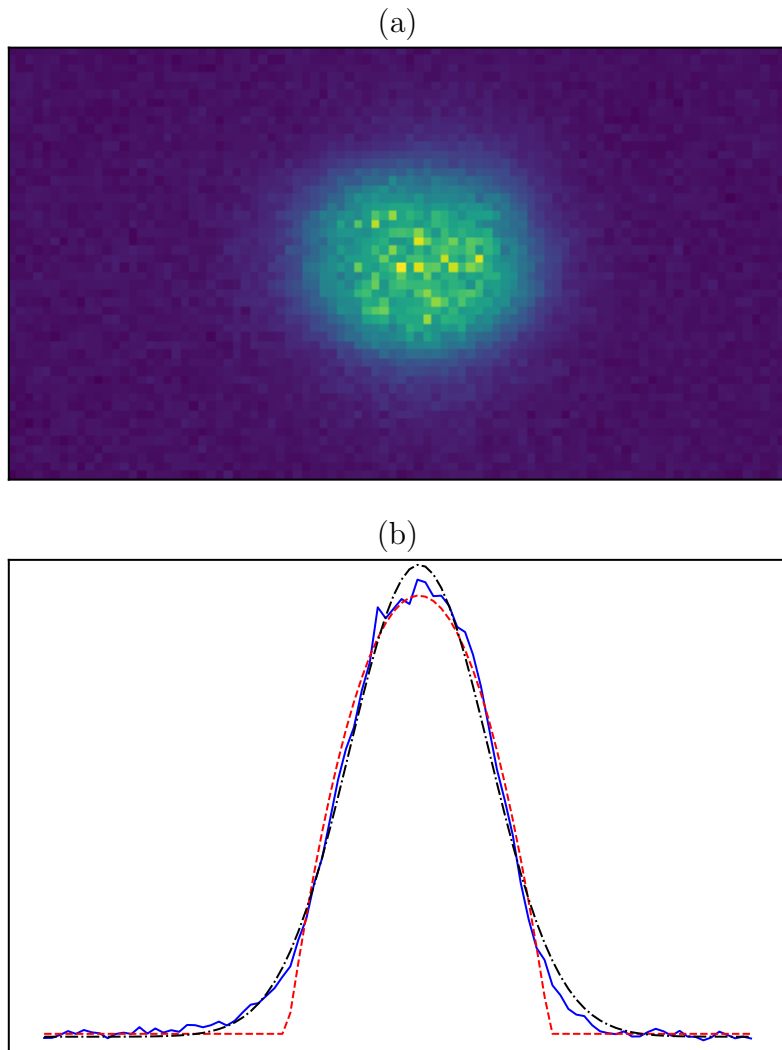


Figure 3: In situ measurement of a fraction of bose condensed atoms. (a) Absorption image taken of $\approx 1\%$ of the cloud. The x and y axes represent x and y position, while color represents the atom number. (b) The blue line represents atom number as a function of position along the x axis, integrated over the y axis. The black dashed line represents the best fit of a Gaussian function to the atomic distribution. The dashed red line represents the best fit of a Thomas-Fermi profile to the atomic distribution.

2.2 Degenerate Fermi Gas

2.2.1 Fermi statistics and the onset of degeneracy

The occupation of different energy levels by Fermions is given by the Fermi-Dirac distribution:

$$n(\epsilon) = \frac{1}{e^{(\epsilon-\mu)/k_B T} + 1}. \quad (2.20)$$

The difference from the Bose-Einstein distribution is simply the sign of the 1 in the denominator. This has important implications, however. First, since e^x varies between 0 and inf, the occupation $n(\epsilon)$ varies between 1 and 0 - a consequence of the Pauli exclusion principle. Second, as the temperature T tends towards 0, there become two distinct cases: $\epsilon - \mu > 0$ and $\epsilon - \mu < 0$. If $\epsilon - \mu > 0$, $e^{(\epsilon-\mu)/k_B T}$ tends towards inf, and $n(\epsilon)$ tends towards 0. If $\epsilon - \mu < 0$, $e^{(\epsilon-\mu)/k_B T}$ tends towards 0, and $n(\epsilon)$ tends towards 1. Therefore, at $T = 0$, the energy states below the chemical potential μ are maximally occupied (with probability 1) and the energy states above the chemical potential are unoccupied.

We can use this to determine the chemical potential at $T = 0$ by constraining the total atom number:

$$N = \sum_j n(E_j) = \sum_{\epsilon_j < \mu} 1. \quad (2.21)$$

Again, we take the common example of the 3-D harmonic trap. Then the task reduces to simply finding the number of energy levels at or below a certain energy μ . This is given by eqn. 2.5. From this, we find the chemical potential at zero energy, which is known as the Fermi energy E_F , as

$$E_F = (6N)^{1/3} \hbar \bar{\omega}, \quad (2.22)$$

where $\bar{\omega} = (\omega_x \omega_y \omega_z)^{1/3}$ is the geometric mean of the three trapping frequencies.

From the Fermi energy, we can define the associated Fermi temperature T_F as

$$T_F = \frac{(6N)^{1/3} \hbar \bar{\omega}}{k_B}, \quad (2.23)$$

and the Fermi momentum $\hbar k_F$ as

$$\hbar k_F = \sqrt{2mE_F}, \quad (2.24)$$

where m is the mass of the Fermion.

For higher temperatures, we can solve for the chemical potential, or the fugacity ζ , by integrating the Fermi-Dirac distribution weighted by the density of states (eqn. 2.6) to obtain

$$N = \int_0^\infty \frac{\epsilon^2}{2\hbar^3 \bar{\omega}^3} \frac{\zeta}{e^{\epsilon/k_B T} + \zeta} = -\frac{(k_B T)^3}{\hbar^3 \bar{\omega}^3} Li_3(-\zeta), \quad (2.25)$$

where Li_3 is again the polylogarithm function. Again, this is a transcendental equation that can be solved numerically. However, in contrast to the BEC case, we do not have to consider the ground state occupation separately, as it is bounded by 1 like every other state.

We show an example of the occupation distribution for different temperatures in Figure 4. Here, we have used the same parameter values as for the BEC case: $N = 10^6$ and $\omega_x = \omega_y = \omega_z = 2\pi 50$ Hz. The Fermi temperature for these parameters is $T_F = 436$ nK. For illustrative purposes, we plot $n(\epsilon)$, unweighted by the density of states $g(\epsilon)$. At zero temperature (red line in the figure), only states below the Fermi energy are occupied. At higher temperatures, the distribution is smoothed out (green and orange lines) until at the Fermi temperature there is almost no significance to the Fermi energy.

In contrast with Bose-Einstein condensation, the transition to a Degenerate

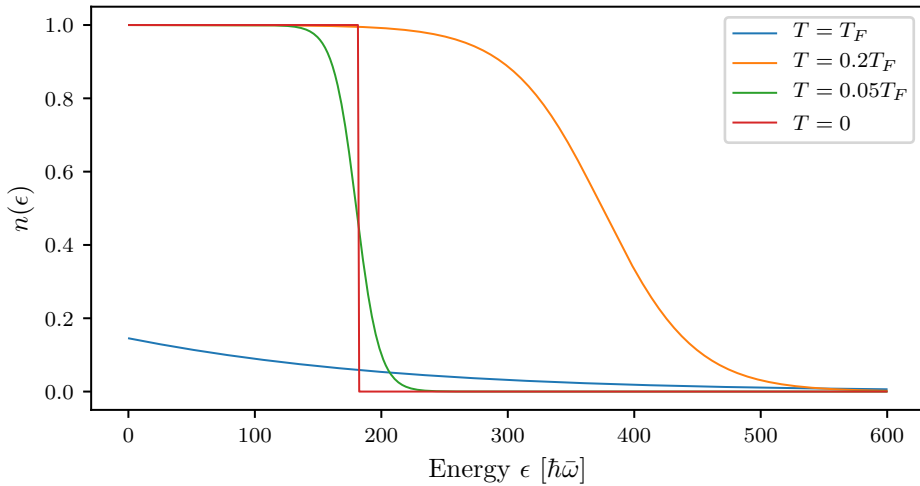


Figure 4: Occupation number as a function of energy for a Fermi gas of $N = 10^6$ atoms in a 3-D harmonic oscillator with frequencies $\omega_x = \omega_y = \omega_z = 2\pi 50$ Hz. The Fermi temperature for these parameters is $T_F = 436$ nK.

Fermi Gas (DFG) is not a phase transition, and there is no absolute measure of the onset of degeneracy. Instead, a Fermi gas can be considered degenerate when the occupation function $n(\epsilon)$ differs significantly from that of a thermal gas. This occurs when the temperature is of order $0.2T_F$.

2.2.2 Interactions and Feshbach resonances

Although the magnitude of the contact interaction U_0 for DFGs is not intrinsically different from that of BECs. There are, however, two key differences. First, the Pauli exclusion principle forbids s -wave interactions between atoms of the same spin. Higher partial wave interactions are 'frozen out' at low temperatures, when the impact parameter of the collision becomes larger than the effective cross section of interactions (see [1], sec. 2.1.2). Therefore, in order to observe interactions, and indeed to cool the gas to degeneracy, another species needs to be present so that intraspecies s -wave interactions can occur. This can be a different atomic species or a different spin state of the same atom.

Second, the densities of standard DFGs ($\approx 10^{12}$ atoms/cm 3) are much lower than that of BECs ($\approx 10^{14}$ atoms/cm 3). Since the likelihood of two-body collisions is proportional to the atomic density ρ^2 , this leads to a much smaller effect of interactions in DFGs.

A widely used technique for enhancing interaction effects in DFGs is Feshbach resonances. A Feshbach resonance occurs between two species (either atomic species or spin species of the same atom) when the open channel, ie the two particles independently in their external potential, energetically approaches a closed channel, ie a bound molecular state of the two species, shown schematically in Figure 5a.

Generally, the atoms in an open channel are energetically sensitive to a background magnetic field B via the hyperfine interaction $H_B = \mu \cdot B$, where μ is the magnetic dipole moment. Tuning the magnetic field should therefore tune the energy of the open channel. The molecular bound state may also have an overall magnetic moment, but it is generally not identical to that of the two atoms in the open channel, and therefore varies differently with the background field. Figure 5b shows an example where the bound state has zero magnetic moment. Here, the energy of both the closed and open channel as a function of background magnetic field B is plotted in the vicinity of a Feshbach resonance. The resonance occurs at a field B_0 where the energies of the two channels coincide.

Assuming there is at least infinitesimal coupling between the closed and open channels, as the energies of the two channels approach each other the perturbative correction term to the energy grows and the interaction between the atoms is effected. This is most easily seen in the s -wave case through changes the scattering length a . In the case where there are no inelastic two-body channels, such as for the ${}^{40}\text{K}$ resonance discussed in this thesis, the interatomic scattering length as a

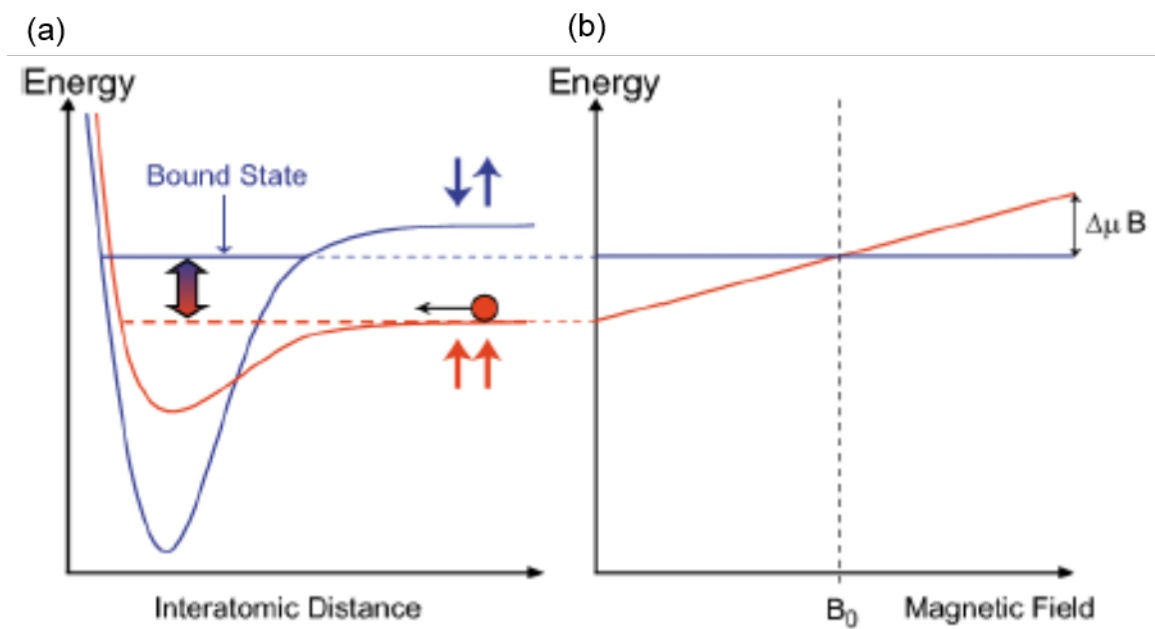


Figure 5: Schematic of a Feshbach resonance. (a) Pictoral representation of energy as a function of interatomic distance for an open channel (red) and closed channel (blue). (b) Energy as a function of background magnetic field B for the closed (blue) and open (red) channels. The energies coincide at the Feshbach resonance point B_0 . Energy of Figure taken from [1].

function of background field is given by [21]

$$a(B) = a_{\text{bg}} \left(1 - \frac{\Delta}{B - B_0} \right), \quad (2.26)$$

where a_{bg} is the background scattering length, Δ is the width of the resonance, and B_0 is the field value at which the resonance occurs. The scattering length diverges at the resonance.

The tunability of interactions provided by Feshbach resonances has allowed for creation of molecular Bose-Einstein condensates from Fermi gases [?, ?, ?] as well as observation of the phase transition from the Bardeen-Cooper-Schrieffer (BCS) superconducting regime to the BEC regime at sufficiently low temperatures [?, ?, ?, 11].

2.3 RbK apparatus

The rubidium-potassium (RbK) apparatus at NIST Gaithersburg has been previously detailed in [?, ?, 7]. In this thesis, we will give a brief overview of the apparatus and how it is used to produce BECs of ^{87}Rb and DFGs of ^{40}K , and only give detailed documentation for those parts of the apparatus that differ from previous works.

A photograph of the main experiment is shown in Figure 6. This is mounted on an optical table, with the science chamber elevated above the surface of the table. The atoms start at the ovens (off to the right, not in the photograph) and travel down the Zeeman slower until they are trapped in the science chamber. The optical dipole trap laser, as well as the 1-D optical lattice laser, are located on the optical table and coupled into optical fibers, which are output on the main floor of breadboard before being sent towards the atoms. All other lasers are located on other optical table and brought over to the experiment table via optical fibers.

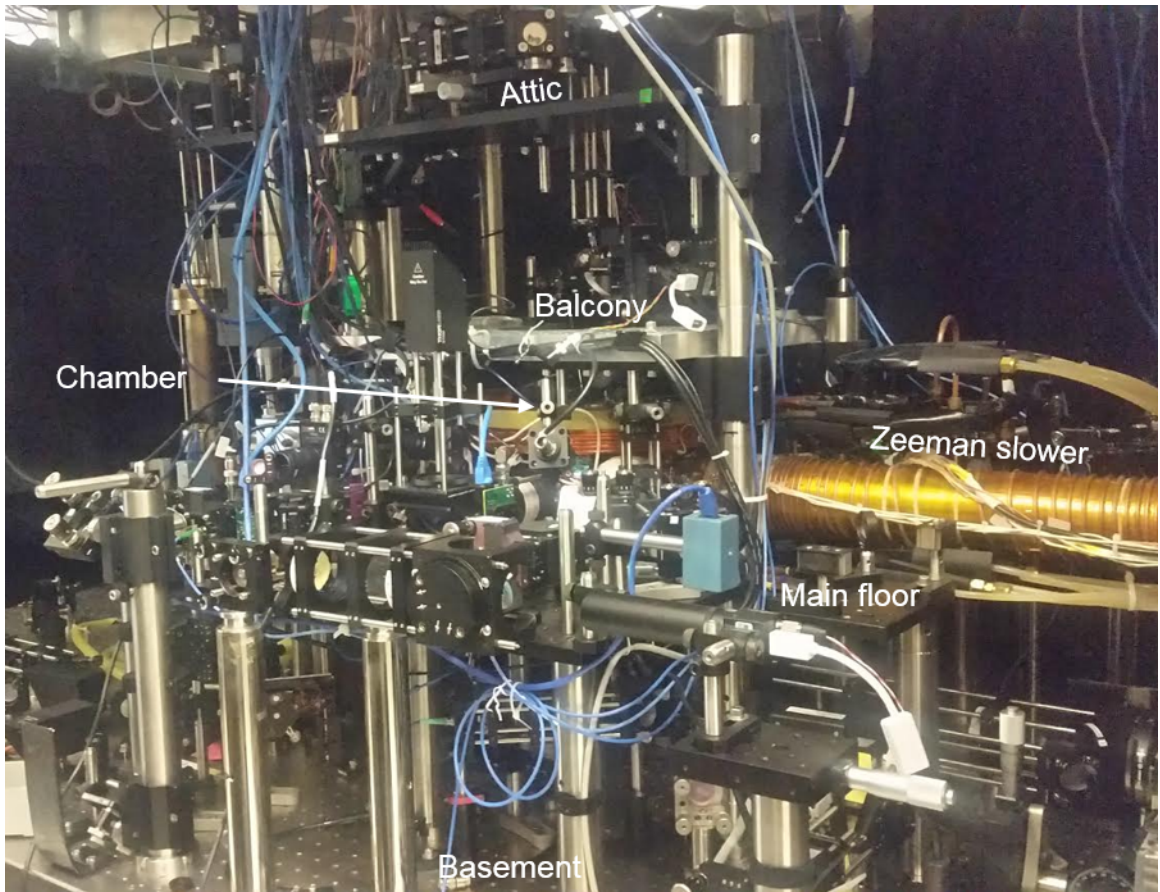


Figure 6: Photograph of RbK apparatus at NIST Gaithersburg. The main science chamber is at the center, hidden behind optics and coils. The Zeeman slower connects the atomic ovens (not shown) to the chamber. There are several levels of breadboards on which optics are mounted, labelled here as basement (surface of optical table), main floor, balcony and attic.

2.3.1 Laser beams

Figure 7 details the beam paths of the light going through the atoms. Figure 7a shows a side view of the apparatus. The up and down going MOTcooling beams are shown in red, reaching the atoms when the flipper mirrors M_{top} and M_{bottom} are flipped in. The down going probe beam, used for imaging along the $x - y$ axis both in situ and in time-of-flight, is shown in solid blue. The probe beam is split via a polarizing beam splitter cube to allow for both in situ and time-of-flight imaging of the same cloud, shown in the inset in fig. 7b and described in greater detail in sec. 2.3.4. The dashed blue line represents the upward going probe beam introduced for alignment purposes, described in greater detail in sec. 2.3.4. The kinematic base mirror (green in the figure) is removable, and only inserted when the alignment beam is in use.

Figure 7b show's a bird's eye view of the apparatus, with optics on the main floor breadboard. The slower cooling (solid dark blue) and slower repump (dashed dark blue) are coming in from the left to slow the atoms as they are moving through the Zeeman slower. The remaining four MOT cooling beams, coming from four opposing directions, are shown in red. They reach the atoms when their flipper mirrors, $M1 - 4$, are flipped in. All six flipper mirrors are computer controlled by the same digital channel, so they can be flipped in and out together. Only the beams going in through mirrors $M1$ and $M2$ are accompanied by MOT repump light, dashed red lines. The repump light for ^{87}Rb (both MOT and slower) comes from a Toptica DL-100 laser. The cooling light (MOT, slower) as well as imaging beams, come from a Toptica TA-100 tapered amplifier system. Both laser are frequency referenced against a master laser, a toptica DL-pro, which is frequency stabilized to a ^{87}Rb atomic transition via saturation spectroscopy (see section 2.3.4).

The optical dipole trap beams (solid green) come from the same 1064 nm laser

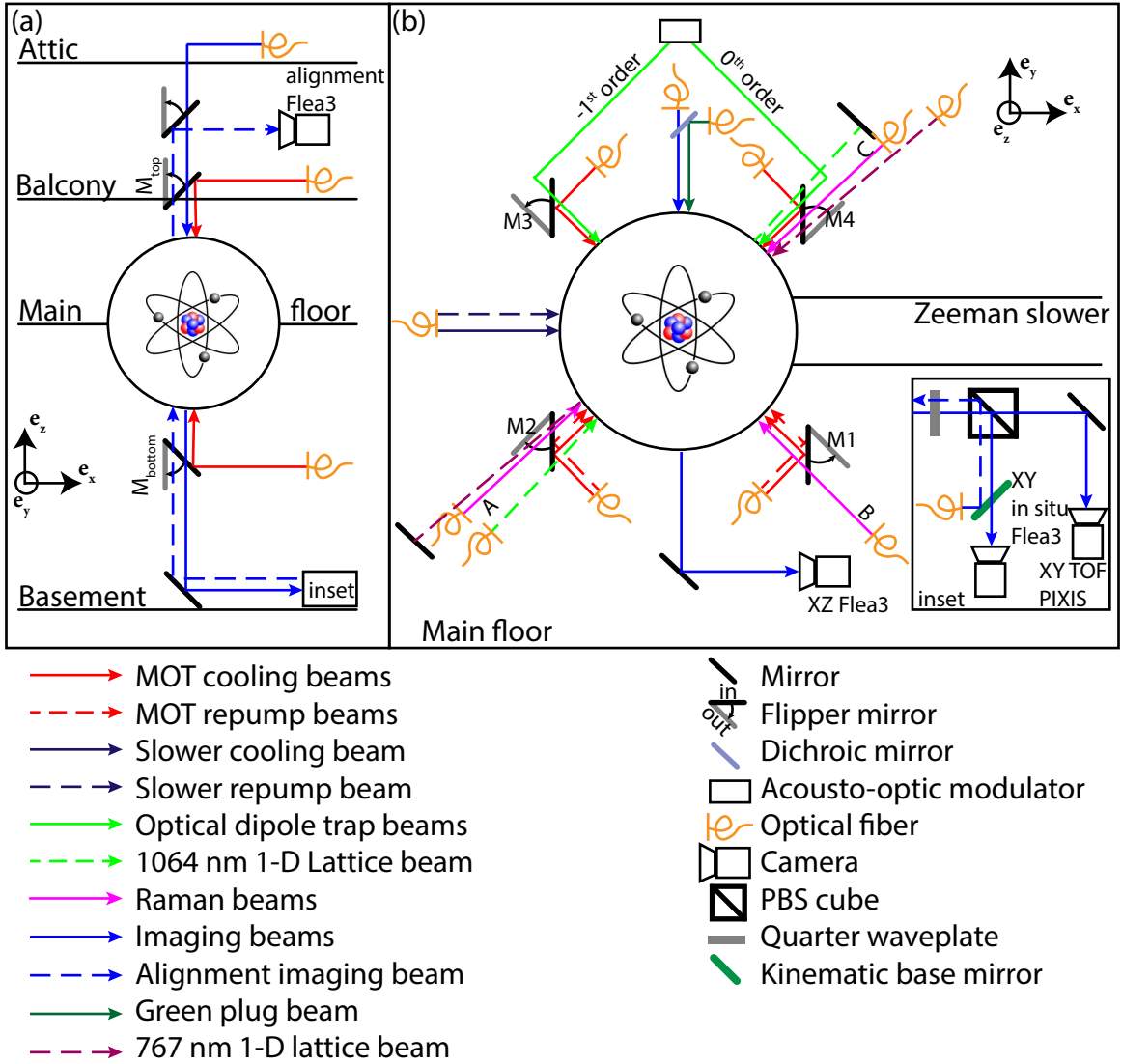


Figure 7: Schematic of RbK apparatus. (a) Side view of apparatus. Only beams propagating along the e_z direction through the atoms are pictured. (b) Top view of apparatus. Only beams propagating along the x - y plane are shown. Schematic is not to scale and the angles are approximate.

(IPG YDL-30-LP), and are split via an acousto-optic modulator into two orders, which enter from opposite directions and intersect each other at approximately a 90 degree angle, providing confinement along all three axes. There is a 1-D optical lattice beam (dashed green), also 1064 nm (IPG YAR-10K-1064-LP-SF, seeded by a pick off from an NPPhotonics seed laser), sent in past the $M2$ mirror and retroreflected on the opposite end of the chamber to form a standing wave pattern. This was also used for experiments in Chapters ???. There is also another imaging beam, imaging the atoms along the x - z plane, going to a Flea3 camera.

There are three available Raman beams (solid magenta): Raman A, entering past the flipped-out $M2$ mirror, Raman B, at 90 degrees to Raman A entering past the $M1$ mirror, and Raman C, counter-propagating with Raman A and entering past the $M4$ mirror. The Raman beams are derived from a tunable Coherent MBR-110 Ti:Sapphire laser seeded by a Coherent Verdi V-10 laser. For experiments described in Chapters ???, we used the Raman A and C beams.

When ^{40}K atoms are in use, the slower cooling, slower repump, MOT cooling, MOT repump and imaging beams are all a combination of frequencies for both ^{87}Rb and ^{40}K , fiber coupled before they were sent to the main experiment table. Both the ^{40}K cooling and repump lasers are Toptica TA-pro systems, with the repump laser frequency stabilized to the ^{40}K atomic transition. In addition, a green plug beam (solid dark green in 7b) is used (see section 2.3.5), derived from a Coherent Verdi V-5 laser. For ^{40}K experiments detailed in Chapter ??, we used a near resonant retroreflected optical lattice beam, shown in dashed dark magenta entering past the $M4$ flipper mirror, coming out past the $M2$ mirror before getting retro-reflected.

2.3.2 Magnetic coils

Figure 8 is a schematic depiction of all the coils used to produce magnetic fields on the RbK apparatus. The quad coils (orange in the figure) are a large pair

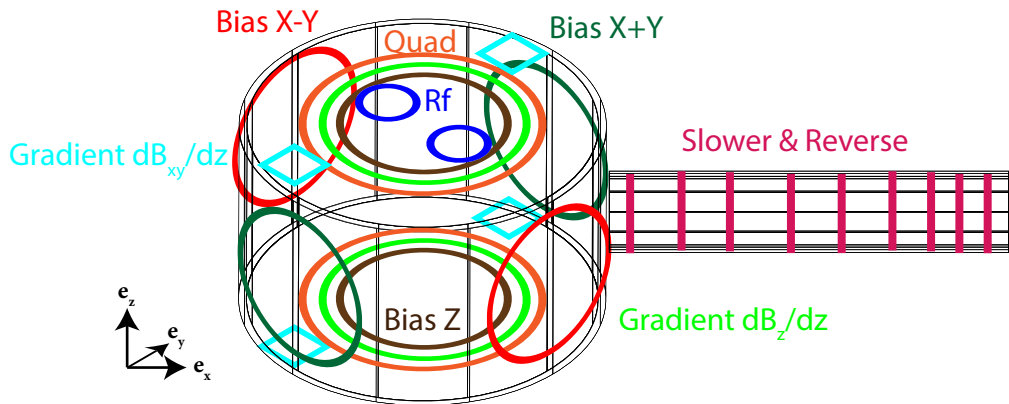


Figure 8: Schematic of magnetic coils on the RbK apparatus. The black wire frame represents the main experiment chamber, with the Zeeman slower off to the right. The Zeeman slower and reverse coils are wound around the Zeeman slower in varying spatial frequency (magenta). The quad (orange), gradient cancellation dB_z/dz (bright green) and biasZ (brown) are all pairs of identical coils on the top and bottom of the apparatus. Bias X-Y coils (red) are a pair of identical coils around the axes of the M_1 and M_3 mirrors, and the bias X+Y (dark green) are a pair of identical coils around the axes of the M_2 and M_4 mirrors. The rf coils (blue) are a pair of circular coils on top of the experimental chamber, spaced enough to allow the top MOT beam through. The gradient cancellation coils dB_{x+y}/dz (cyan) are four square coils on top and bottom of the experiment along the X+Y axis.

of coils used to produce a quadropole field for the MOT. The top and bottom coils are connected through four IGBT switches, forming an h-bridge. This allows switching between two configurations: anti-Helmholtz and Helmholtz. In anti-Helmholtz configuration, the top and bottom coils conduct current in opposite directions, producing a quadrupole field gradient at the center. This is the configuration used for the MOT, as well as for producing a Stern-Gerlach gradient for spin resolved imaging. In Helmholtz configuration, the two coils conduct current in the same direction, producing a strong bias field along the e_z direction. This was used to get close to the Feschbach resonance in the experiment detailed in Chapter ??.

There are three pairs of bias coils, used to cancel constant background fields or provide field offsets along the three axes. All three are in Helmholtz configuration. The biasZ coils (brown) are on top and bottom of the experiment and provide a constant B_z field at the center. The biasX+Y coils (dark green) are vertical on two opposite sides of the apparatus along the $e_x + e_y$ directions, and the biasX-Y (red) are on the other two opposing sides along the $e_x - e_y$ directions. There are also two sets of gradient cancellation coils available, although they are not subject to feedback loops or computer control. The first is another pair of coils on top and bottom of the apparatus (bright green), connected in anti-Helmholtz configuration to produce a small gradient dB_z/dz . The second is four square coils mounted above and below each biasX+Y coil (cyan). Both pairs of coils (a pair here is two of the square coils one above the other) are wound in Helmholtz configuration, and the two pairs are in series, providing a small gradient dB_{x+y}/dz at the atoms.

2.3.3 Procedure for making a BEC

In the first step of the BEC making procedure, the atoms starting at the oven are cooled via a Zeeman slower and captured in a Magneto-Optical trap in the siccience chamber. During this step, the Zeeman slower is on, with both the coils and the

slower cooling and repump lights on. These beams (dark blue in Figure 7b) are 7.6 MHz red detuned from the $|F = 2, m_F = 2\rangle$ to $|F = 3, m_F = 3\rangle$ transition of ^{87}Rb (133 MHz beat note offset from master laser). At the same time, the flipper mirrors $M1 - 4, M_{bottom}, M_{top}$ are flipped in and the MOT cooling and repump beams (red in Figure 7) are on. The quad coils are on in anti-Helmholtz configuration with 25 A of current running through them, producing a field gradient of $\frac{dB_z}{dz} \approx 13$ Gauss/cm. This step can be set to take anywhere from ≈ 0.7 s to ≈ 5 s depending on how many atoms are needed.

Next is the optical molasses step, during which sub-Doppler cooling of the atoms occurs. For this step, the Zeeman coils and slower lights are turned off. The quad coil current is also switched off, leaving just the MOT cooling light and only leakage MOT repump light. The MOT cooling light is set to -20.6 MHz below the $|F = 2, m_F = 2\rangle$ to $|F = 3, m_F = 3\rangle$ transition (120 MHz beat-note command). It is then linearly ramped in 19 ms down to a detuning of -90.2 MHz (50 MHz beat-note command). Since the repump light is all but off in this step, the atoms are also depumped into the $F = 1$ manifold. Then, the atoms are optically pumped into the $|F = 1, m_F = -1\rangle$ state to make them trappable by the quadrupole field. This is done by turning on the slower repump beam (dashed dark blue in fig. 7b) 1 ms. Then, the XZ imaging beam (blue in fig. 7b) is briefly turned on to get rid of any remaining $F = 2$ atoms.

Next, we compress the atoms and perform forced Rf evaporation. To compress, the quad coils are first turned on to 130 A. After holding for 20 ms, we sweep the current linearly to 250 A in 200 ms. The forced rf evaporation is then performed by turning on the rf coupling field and sweeping the frequency from 20 MHz to 4 MHz in 4 s to couple the highest energy atoms from $|F = 1, m_F = -1\rangle$ to $|F = 1, m_F = 0\rangle$ and allow them to escape the trap. The slow ramp is designed to allow the system to rethermalize through collisions as the hottest atoms are ejected. During rf evap-

oration, the crossed optical dipole trap (ODT) is on at an initial command power of 2.0 and initial split (command to AOM controlling the power split between the two crossing beams, shown in fig. 7b) of 0.01. This allows any atoms that are cold enough to see the optical trap to be captured by it.

Then, the atoms are decompressed and loaded into the ODT. The quad current is ramped down to 60 A exponentially with a time constant of $\tau = 1.5$ s in 3 s. This is the quad current at which the atoms are only barely suspended against gravity by the quadrupole trap. At the same time, the biasZ current is ramped down from 10 A to 8 A, lowering the center of the quadrupole trap to the ODT. Then, the atoms are evaporated in the ODT. This is done over the course of 5 s, ramping down the depth of the ODT and allowing the hottest atoms to escape. During this step, the ODT power is ramped exponentially from the initial command of 2.0 to a final command of 0.4, while the split command is ramped up linearly from 0.01 to 0.65, effectively turning on the crossing -1^{st} order beam. It is during this evaporation step that the atoms are cooled below the critical temperature and condensed.

Finally, the quad current is ramped exponentially to 0 A in 5 s, leaving the atoms optically trapped. Then any desired experiment can be performed on the BEC. For daily checks of the BEC, no experiments are performed and the atoms are released from the trap and allowed to expand in time-of-flight for 16.2 ms before being absorption imaged in the XY plane by the PIXIS imaging camera, pictured in fig. 7b.

2.3.4 Changes to apparatus for Rubidium

In this section, we describe a few of the changes that were made to the apparatus since the writing of Lauren Aycock's thesis [?]. This is not an exhaustive list, but rather the most notable changes to the main setup affecting BEC production.

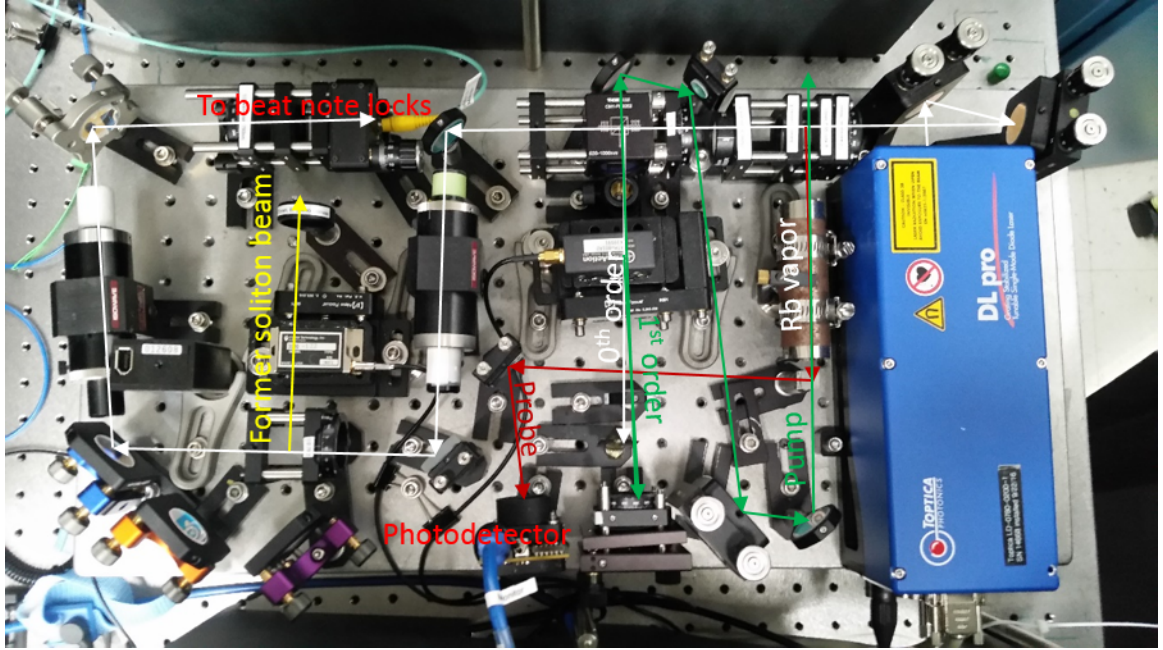


Figure 9:

2.3.4.1 Master laser setup

In 2014, the master laser board was replaced by a new version, with a new laser that was not dying. The laser was a Toptica DL-Pro, and it output approximately 80 mW, allowing for an extra beam arm that was used to

2.3.4.2 Alignment imaging path

2.3.4.3 ODT beam shaping

In 2015, two projects were being carried out on the apparatus at the same time: Lauren's soliton project [PUT REFERENCE TO PAPER HERE] and the synthetic dimensions project detailed in chapter ???. The soliton project used an elongated BEC, requiring the dipole trap to be highly elongated along one direction, here $e_x + e_y$. For this, only the 0th order of the ODT was used and it was made very tight both along the horizontal and vertical directions: with 42 and 55 μm waists, respectively. The synthetic dimensions projects suffered from momentum changing collisions, and

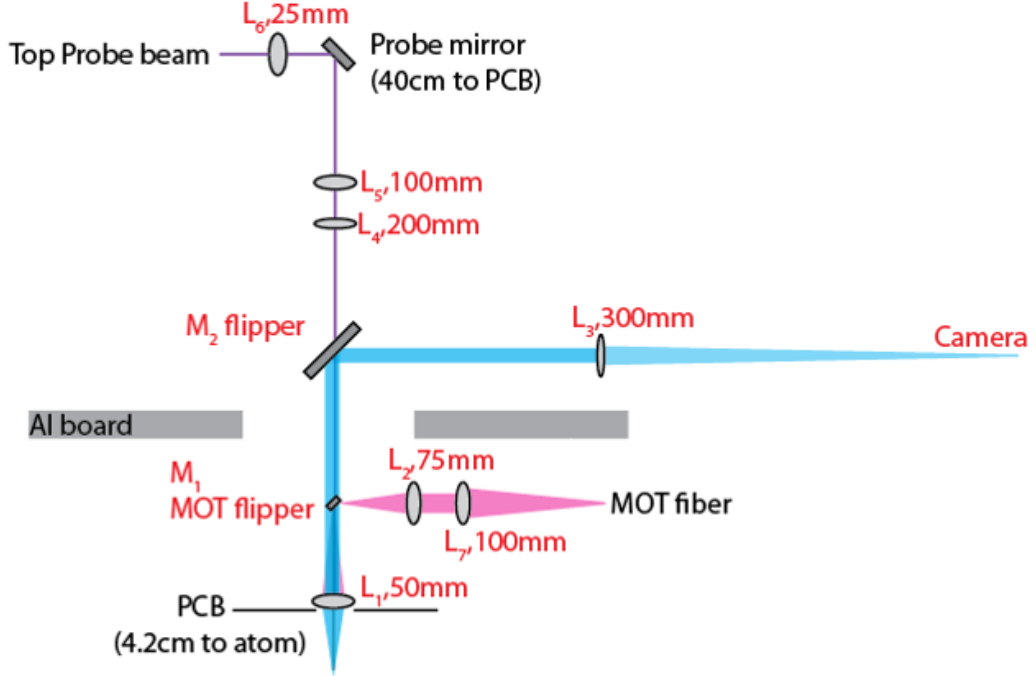


Figure 10:

therefore needed the cloud to be as dilute as possible. For this, the 0th order ODT beam still needed to be tight in the vertical direction to suspend against gravity, but needed to be as wide as possible (while still retaining a detectable atom number) in the horizontal. Therefore, an extra cylindrical lens on a removable, rotatable mount was added in the beam path to switch between the two configurations.

The location of this new lens is detailed in Figure 12. Without this lens, the beam was sent through a telescope (the $f = 10$ and $f = 15$ cm lenses [DOESNT MAKE SENSE CHECK IF ONE IS DIVERGENT]) before reaching an $f = 25$ cm focusing lens, placed 25 cm away the center of the chamber to focus the beam at the atoms. The beam waist as a function of propagation distance along this beam path is shown in blue in Figure 13 a. This graph was made by Dr. Ian Spielman from a python calculation of gaussian beam optics. According to the calculation, the beam is focused down to a $45 \mu\text{m}$ waist at the atoms located at a displacement

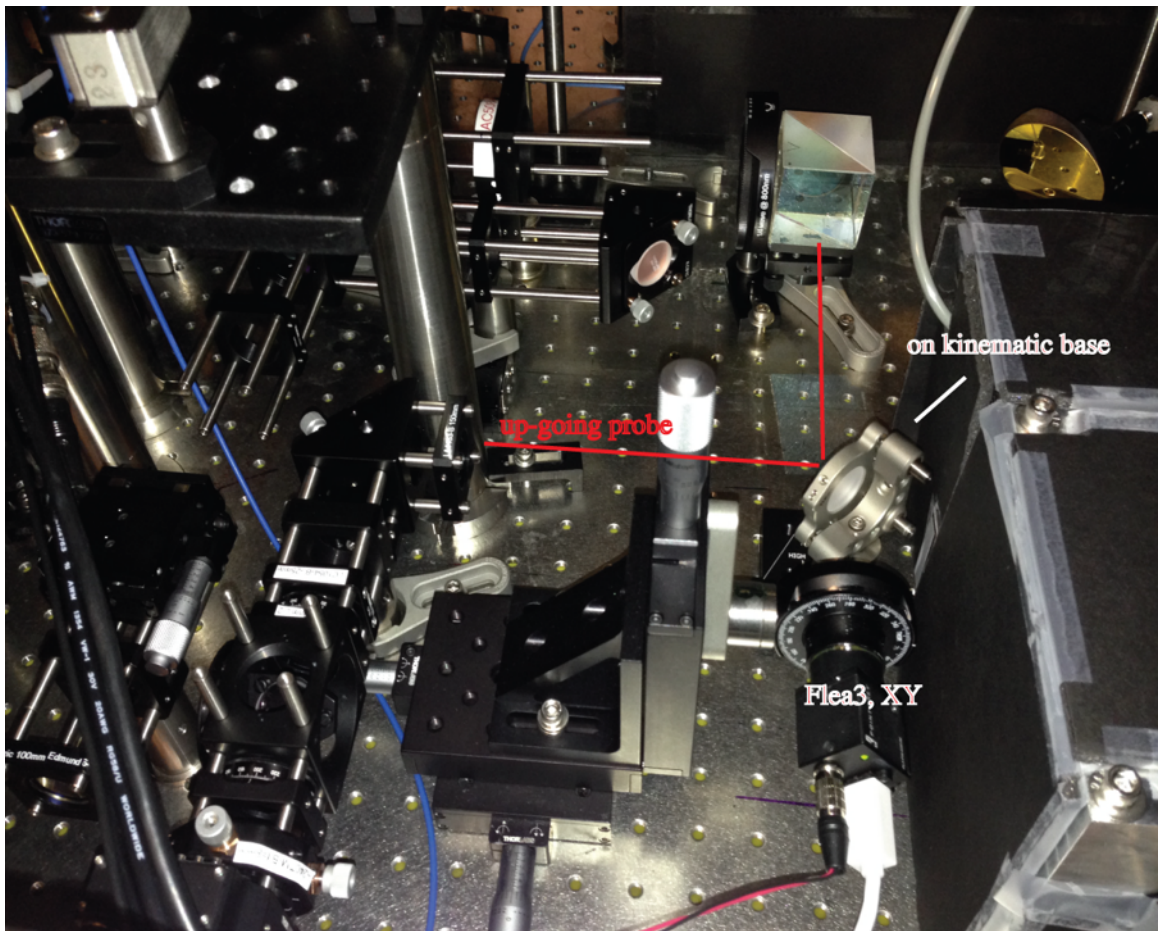


Figure 11:

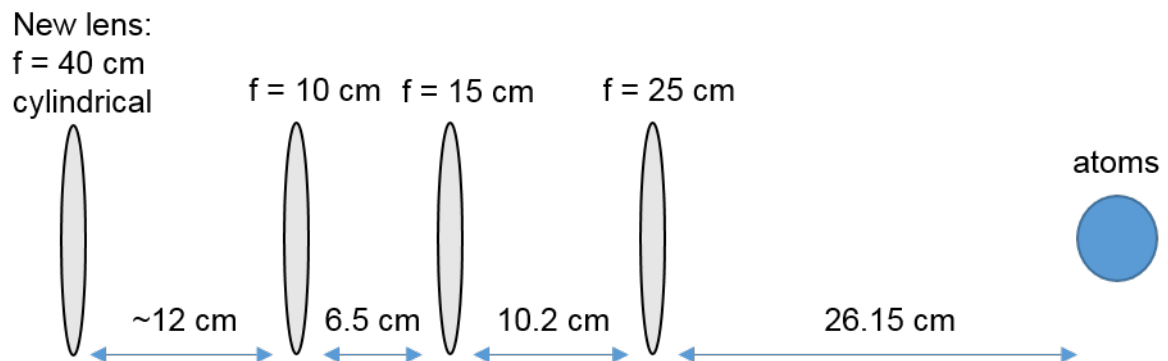


Figure 12: Schematic of beam shaping optics in the path of the 0th order ODT beam, after the split AOM. The new lens, on a removable mount, is cylindrical, shaping the beam along the horizontal axis only.

of 1400 mm.

The additional lens used was an $f = 40$ cm cylindrical lens, rotated in its rotating mount to focus the beam slightly in the horizontal direction. The effect of this lens on the horizontal beam waist along its path was calculated and plotted (again by Ian using his code) in Figure 13 b. This plot was made for a $f = 75$ cm lens instead of $f = 40$ cm, but the qualitative effect is the same. As seen in the figure, the waist of the beam is not significantly impacted by the addition of the lens, but the focus is shifted away from the atoms, resulting in a larger waist at the atoms. The horizontal beam waist at the atoms with the $f = 40$ cm lens as measured by a beam profiler camera was $115 \mu\text{m}$. This was the configuration used in the experiments described in Chapter ??.

2.3.5 Procedure for making a DFG

To make a degenerate Fermi gas of ${}^{40}\text{K}$, we followed a similar cooling procedure as for making a BEC, with some key differences. First, as mentioned in sec. 2.2.2, due to the Pauli exclusion principle, spin polarized ${}^{40}\text{K}$ atoms cannot undergo s -wave collisions, and therefore below a certain temperature have no method to thermalize on their own and cannot be evaporatively cooled. To overcome this problem, we cooled a mixture of ${}^{87}\text{Rb}$ and ${}^{40}\text{K}$, effectively using ${}^{87}\text{Rb}$ as a collision mechanism to allow the Fermions to thermalize. Second, ${}^{40}\text{K}$ is slightly below half the mass of ${}^{87}\text{Rb}$. This leads to a larger magnitude of transverse velocity for ${}^{40}\text{K}$ atoms in the Zeeman slower, leading to a larger fraction of atoms missing the capture region of the MOT. To mitigate this issue, we utilized transverse cooling of ${}^{40}\text{K}$ before the Zeeman slower. This consisted of two pairs of counter-propagating beams along the $e_z + e_y$ and $e_z - e_y$ directions, performing Doppler cooling in the directions perpendicular to propagation (not shown in fig. 7b). The lower mass of ${}^{40}\text{K}$ also leads to a larger number of Majorana losses near the center of the MOT: spin flips

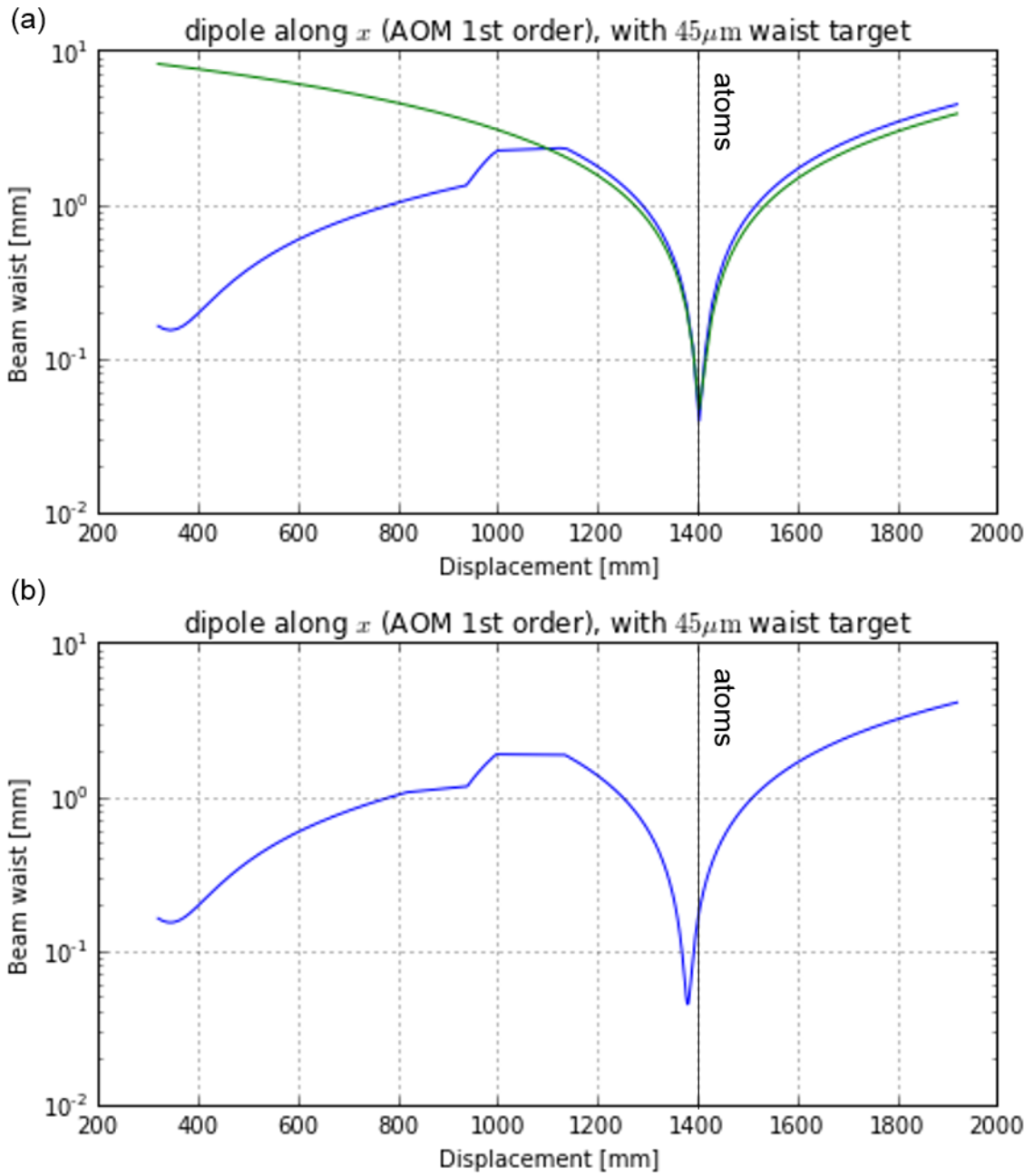


Figure 13: Beam waist as a function of propagation distance as calculated by Ian Spielman's code. Graphs also made by Ian Spielman. The atoms are at displacement = 140 cm. (a) Without additional lens. Blue line represents horizontal beam waist. (b) With an additional $f = 75$ cm lens 12 cm in before the next optic.

that take the atoms out of the trappable states because they are moving too fast to adiabatically follow the changing magnetic field direction [?, ?, ?]. To mitigate this issue, for cooling ^{40}K the center of the quadrupole trap was plugged by a tightly focused green (repulsive) laser beam (dark green in fig. 7b).

First, ^{40}K atoms starting at the oven were cooled via a Zeeman slower and transverse cooling and captured in a MOT for 7 s. Then, both ^{40}K and ^{87}Rb atoms were slowed and MOT loaded for 1.5 s. The subsequent optical molasses step was only 2 ms long, with the ^{87}Rb MOT cooling light ramped linearly from -20.6 MHz below the $|F = 2, m_F = 2\rangle$ to $|F = 3, m_F = 3\rangle$ transition (120 MHz beat-note command) to -40.6 MHz away from resonance (100 MHz beat-note command). In this time, the ^{40}K cooling light was turned down in intensity but the detuning remained unaltered.

Next, ^{87}Rb was optically pumped into the $|F = 2, m_F = 2\rangle$ state using the slower cooling beam, while ^{40}K was optically pumped into the $|F = 9/2, m_F = 9/2\rangle$ state using a dedicated optical pumping beam in $250\mu\text{s}$. These are magnetically trappable states, and we subsequently turned on the quad coil current to 130 A to capture the atoms in the magnetic trap, along with the green plug beam at the center to prevent Majorana losses. Both species were compressed by a linear ramp of the quad current up to 160 A in 0.5 s. Then, forced rf evaporation was performed for 10 s, sweeping the rf frequency linearly from 18 MHz down to 2 MHz.

Then, the atoms were decompressed and loaded into the ODT, similarly to the BEC procedure. The ODT was turned on to an initial power of 2 and an initial split command of 0.01. The quad current was ramped down to 25.5 A exponentially with a time constant of $\tau = 1.5$ s in 3 s. The evaporation in the ODT was split into two steps. During the first 3 s step, the split was ramped linearly to its final command power of 0.65, putting more power into the (less tightly focused) crossing beam. The green plug beam was ramped off during this step. During the second, 4

s step, the overall power of the ODT was exponentially ramped down to [CHECK THE INTERMEDIATE ODT COMMAND FOR K], while the quad coil current was ramped exponentially to 0.

We then used adiabatic rapid passage (ARP) to transfer the ^{87}Rb atoms from $|F = 2, m_F = 2\rangle$ to $|F = 1, m_F = +1\rangle$ using a microwave coupling field and a 50 ms ramp in biasZ coil current. Then, we pulsed on the XZ imaging beam to eject any remaining $F = 1$ atoms. Then we performed one last evaporation step in the ODT, ramping the final power down to [CHECK THE FINAL ODT COMMAND FOR K]. The ^{87}Rb atoms were no longer suspended against gravity and fell out of the trap. We then were free to perform experiments with the degenerate ^{40}K cloud.

2.3.6 Current status of Potassium apparatus

At the time of writing, the ^{40}K part of the apparatus as described is no longer functional. The number of ^{40}K atoms collected in the MOT has started decaying significantly in January 2014, and by March was almost completely gone and could not be resurrected. The specific failure point of the setup was not clear. However, other groups have found that atomic sources are much more stable, and a higher fraction of the (expensive) ^{40}K sources can be utilized when the atoms were initially cooled with a 2-D MOT rather than a Zeeman slower [?, ?, ?]. Therefore, rather than continuing to attempt to revive the existing set-up, the decision was made to build a 2-D MOT for both ^{40}K and ^{87}Rb .

The design of our 2D MOT is closely based on the design in Thomas Uehlinger's diploma thesis [?]. The design was developed by Dalia Ornelas, and initially implemented by Marcell Gall before it was taken over by the rest of the RbK team. The schematic of the planned vacuum system (with attached optics) is pictured in Figure 14. On the left side of the schematic, there are optics directing the pushing beam into a miniconflat viewport. The viewport is part of a cross, with the ^{40}K and

^{87}Rb ovens attached to the two ends of the cross, with gate valves allowing one to close off one or both sources from the rest of the vacuum system. From there, the cross attaches to the main 2D MOT cell via a mini-conflat flange.

The cell is a custom machined stainless steel frame with rectangular anti-reflection (AR) coated windows on four sides and mini-conflat connectors on two ends, pictured in more detail in Figure 15. Two aluminum mounting crosses attach to either end of the cell. Four aluminum bars are connected between the crosses, and the main 2D MOT optics are mounted on those four bars. The opposite end of the cell (right in fig. 14) sandwiches a differential pumping tube in the mini-conflat connection and connects to another cross. The top of the cross connects to a small ion pump. The bottom connects to a rotatable feed-through mechanism with a 'flag', a square of metal, attached inside. The rotator rotates the flag in and out of the atomic beam path, providing a means of losing off the main chamber from the atomic beam and push beam light. The fourth end of the cross connects to another gate valve, separating the 2D MOT vacuum system from the main experiment chamber. The other end of this valve connects to a flange that is meant to connect directly to the main experiment chamber.

A picture of the stainless cell is shown in Figure 15. Attaching the glass windows to the stainless steel frame in a vacuum tight way proved to be quite difficult, and this picture was taken during one of the attempts to do so using epoxy. The clamps around the cell served to keep the windows in place as the epoxy was curing. In the final design, the seal was made with indium, with gaskets custom machined to press the windows onto the cell. We roughly followed the indium sealing method presented in [?], with gaskets above and below the windows. We also employed pre-squashing, where a metal piece in the shape of the window was first pressed onto the indium wire to flatten it and minimize the amount of pressure that needed to be applied to the glass window.

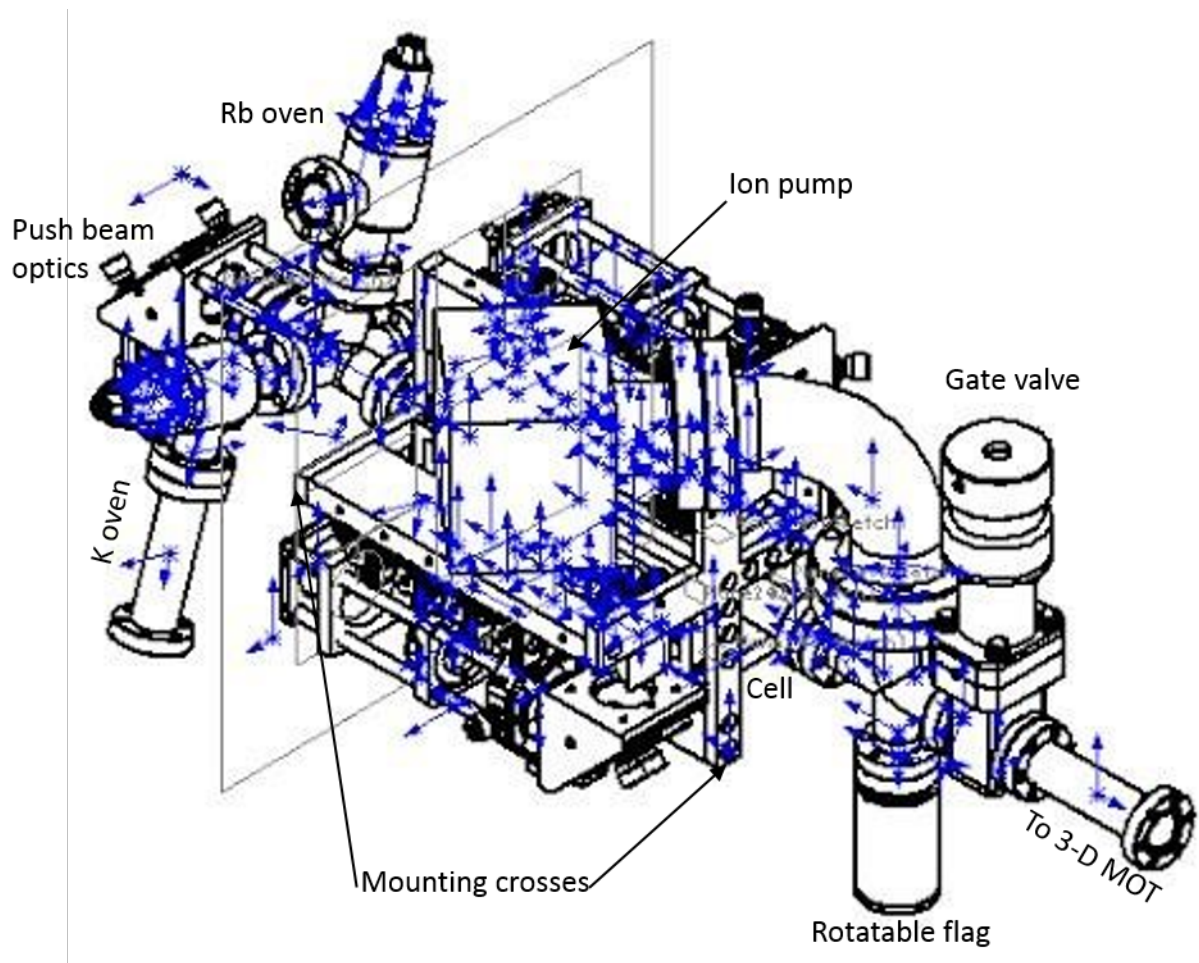


Figure 14: Schematic of the 2D MOT setup. The mini-conflat on the right is to be attached to the existing experiment chamber, directing the atomic beam into the 3D MOT.

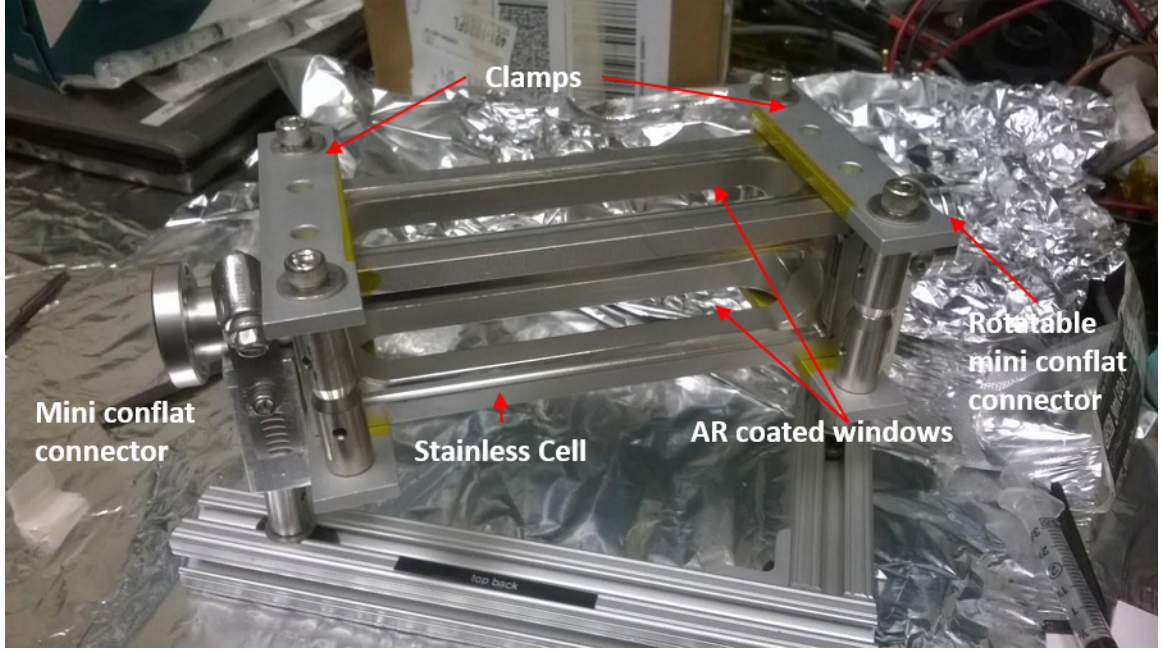


Figure 15: Picture of 2D MOT cell during an attempt to epoxy AR coated windows onto the stainless steel frame. The clamps serve to hold the windows in place while epoxy cures.

The main 2D MOT optics direct the cooling and repump beams into the cell from two directions, and retro-reflect them on the other end, producing cooling along those two directions (hence the name 2D MOT). The optical set-up along one of those directions is presented schematically in Figure 16. The cell is elongated along the atomic beam direction, to maximize the time the atoms are cooled while travelling to the 3D MOT. Because of this, instead of a highly elliptical cooling beam, four MOT beams are launched in a row, almost overlapping, from each of the two directions. This is accomplished by splitting one beam into four with four sequential beam-splitting cubes (BSs).

The 2D MOT cooling and repump light is first periscoped over from a fiber and lens assembly (designed to shape the beam to be roughly 1 inch in diameter). It then goes through a half-wave plate (HWP) before entering the first 70/30 beam splitter. 30% of the light is sent through a quarter-wave plate (QWP) tuned to provide circularly polarized light into the cell. On the other side of the cell, the

beam hits another QWP before being retro-reflected back into the cell. Since the beam hits the QWP on the other side of the cell twice, the circular polarization is preserved. The remaining 70% of the light goes into the next 70/30 BS, sending 21% of the total beam power into the second arm going into the cell, to be retro-reflected in the same way. The remaining 49% hits a 50/50 BS, sending 25.5% of the total beam power into the third retro-reflected arm. The final cube is a polarizing beam-splitter (PBS), and the HWP before the cubes is tuned to ensure all of the light is sent into the cell on this last, fourth, arm.

The push beam enters from the oven direction and serves to provide some velocity to the atoms along the long direction of the cell to ensure they continue to travel to the 3D MOT, while still providing some cooling along the longitudinal direction. In order to provide this cooling, the push beam is also retr-reflected, with the help of a specially machined differential pumping tube (on the right in fig. 16). The differential pumping tube is machined to have a 45° angled polished end, reflecting all of the light except for the central part towards a retro-reflecting mirror outside the cell. Along the other 2D-MOT cooling direction (up and down in fig. 16), this whole set of optics is replicated, with the exception of the push beam retro-reflection.

The current 2D-MOT setup is pictured in Figure 17. The vacuum system has been assembled and successfully pumped down, with a octagonal test chamber in place of the main experimental chamber. This test chamber is intended to be used to send probe light through and detect florescence to characterize the atomic beam coming out of the 2D MOT. The optics have been assembled and the quarter-wave plates lightly epoxied onto the BS cubes and mirrors, although as can be seen in the picture some have regrettably fallen off. Quadropole coils have been wound around each of the four windows, onto 3D printed coil winding forms. BiasZ coils have also been wound to cancel out stray gradients along the atomic beam direction.

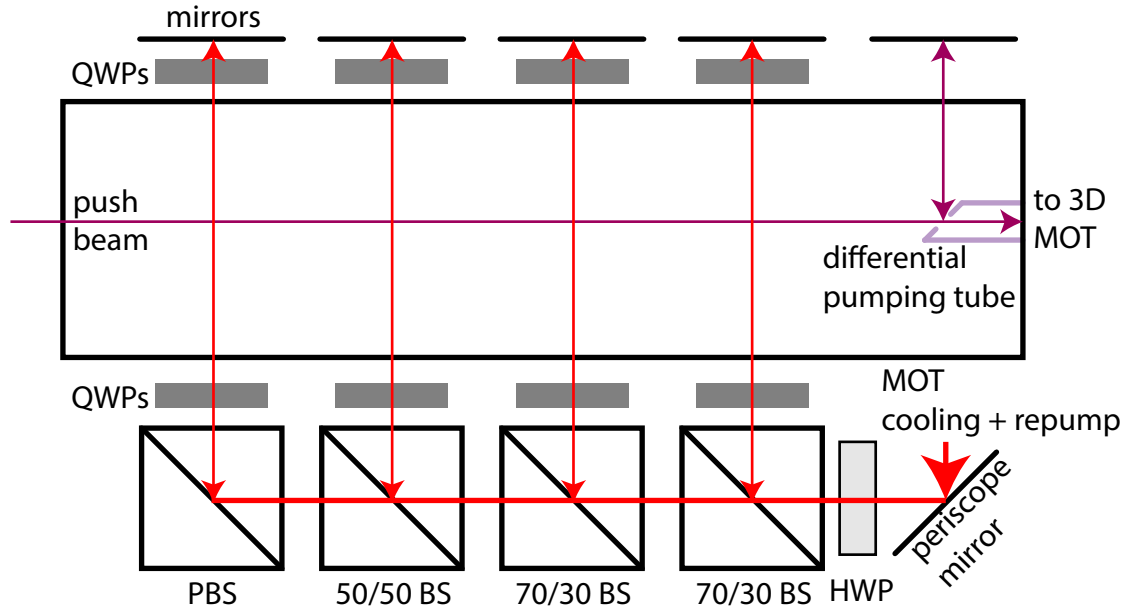


Figure 16: Schematic of 2D MOT optics along one direction. The main cooling and repump beam is split into four parallel arms by four beam splitter cubes. The push beam enters from the oven direction and is retro-reflected via a custom machined and polished differential pumping tube. These optics are mounted on crosses attached to the 2D MOT cell.

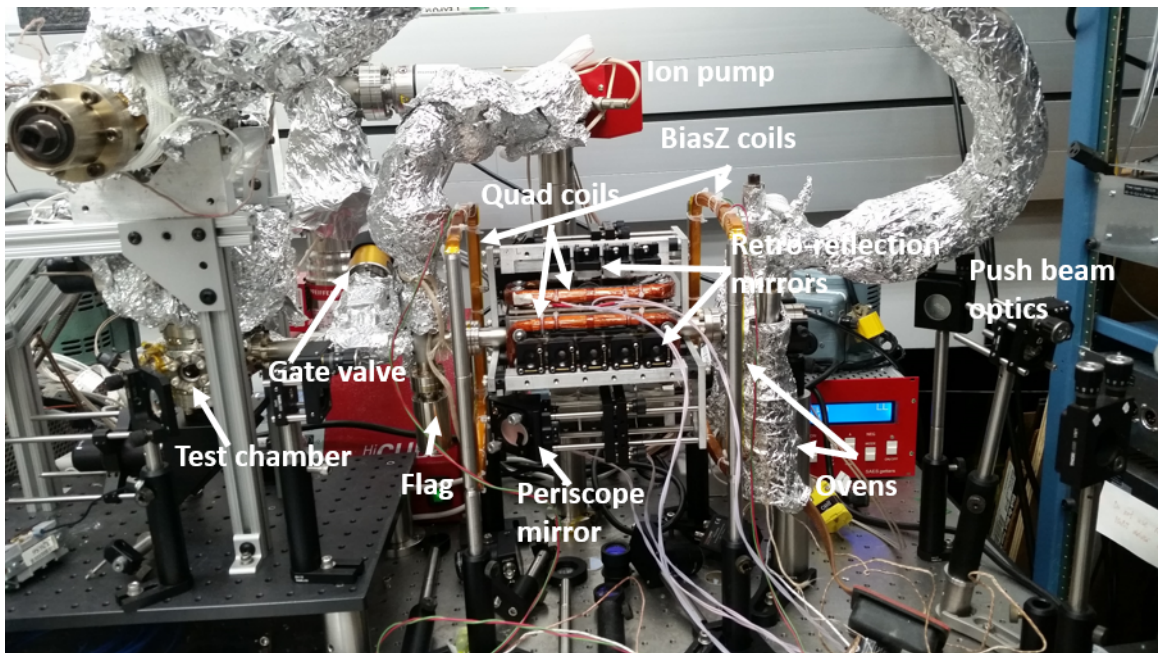


Figure 17: Picture of current 2D MOT apparatus. The vacuum system is in place, optics are (mostly) mounted and coils to generate the quadrupole trap and cancel gradients along the atomic beam direction have been wound.

The two Toptica TA-pro systems that were used to provide all ^{40}K light in the past are still operational, and need to be re-purposed to provide both 2D MOT and 3D MOT cooling and repump light. A new Toptica TA-pro was also purchased, with the intent to implement gray molasses cooling on the $^{40}\text{KD1}$ line as described in [?].

Bibliography

- [1] W. Ketterle and M. W. Zwierlein. Making, probing and understanding ultracold Fermi gases. In *Ultracold Fermi Gases, Proceedings of the International School of Physics ‘Enrico Fermi’, Course CLXIV*, Varenna, 20-30 June 2006.
- [2] Daniel Adam Steck. Rubidium 87 d line data. Available online, <http://steck.us/alkalidata>, April 2018. revision 2.1.5.
- [3] K. Jiménez-García, L. J. LeBlanc, R. A. Williams, M. C. Beeler, A. R. Perry, and I. B. Spielman. Peierls substitution in an engineered lattice potential. *Phys. Rev. Lett.*, 108:225303, May 2012.
- [4] H.J. Metcalf and P. van der Straten. *Laser Cooling and Trapping*. Graduate Texts in Contemporary Physics. Springer New York, 1999.
- [5] N.W. Ashcroft and N.D. Mermin. *Solid State Physics*. Saunders College, Philadelphia, 1976.
- [6] Nicola Marzari, Arash A. Mostofi, Jonathan R. Yates, Ivo Souza, and David Vanderbilt. Maximally localized wannier functions: Theory and applications. *Rev. Mod. Phys.*, 84:1419–1475, Oct 2012.

- [7] Karina Jimenez-Garcia. *Artificial Gauge Fields for Ultracold Neutral Atoms*. PhD thesis, Joint Quantum Institute, National Institute of Standards and Technology, and the University of Maryland, 2012.
- [8] Daniel Adam Steck. Quantum and atom optics. Available online at <http://steck.us/teaching>, January 2015. revision 0.12.2.
- [9] D. Genkina, L. M. Aycock, B. K. Stuhl, H-I Lu, R. A. Williams, and I. B. Spielman. Feshbach enhanced s-wave scattering of fermions: direct observation with optimized absorption imaging. *New Journal of Physics*, 18:013001, Dec 2015.
- [10] Lindsey J. LeBlanc. *Exploring many-body physics with ultracold atoms*. PhD thesis, University of Toronto, 2011.
- [11] C. A. Regal, M. Greiner, and D. S. Jin. Observation of resonance condensation of fermionic atom pairs. *Phys. Rev. Lett.*, 92(4), 2004.
- [12] E. Tiesinga, B. J. Verhaar, and H. T. C. Stoof. Threshold and resonance phenomena in ultracold ground-state collisions. *Phys. Rev. A*, 47(5, B):4114–4122, 1993.
- [13] M. Lysebo and L. Veseth. *Ab initio* calculation of Feshbach resonances in cold atomic collisions: *s*- and *p*-wave Feshbach resonances in ${}^6\text{Li}_2$. *Phys. Rev. A*, 79:062704, 2009.
- [14] B. Gao. Analytic description of atomic interaction at ultracold temperatures. II. Scattering around a magnetic Feshbach resonance. *Phys. Rev. A*, 84:022706, 2011.

- [15] S. Inouye, M. R. Andrews, J. Stenger, H. J. Miesner, D. M. Stamper-Kurn, and W. Ketterle. Observation of Feshbach resonances in a Bose-Einstein condensate. *Nature*, 392(6672):151–154, 1998.
- [16] S. L. Cornish, N. R. Claussen, J. L. Roberts, E. A. Cornell, and C. E. Wieman. Stable Rb-85 Bose-Einstein condensates with widely tunable interactions. *Phys. Rev. Lett.*, 85(9):1795–1798, 2000.
- [17] C. A. Regal and D. S. Jin. Measurement of positive and negative scattering lengths in a Fermi gas of atoms. *Phys. Rev. Lett.*, 90:230404, 2003.
- [18] K. M. O’Hara, S. L. Hemmer, M. E. Gehm, S. R. Granade, and J. E. Thomas. Observation of a strongly interacting degenerate Fermi gas of atoms. *Science*, 298(5601):2179–2182, 2002.
- [19] C. Monroe, E. Cornell, C. Sackett, C. Myatt, and C. Wieman. Measurement of Cs-Cs elastic scattering at $T = 30 \mu\text{K}$. *Phys. Rev. Lett.*, 70:414–417, 1993.
- [20] B. DeMarco, J. L. Bohn, J. P. Burke, M. Holland, and D. S. Jin. Measurement of p -wave threshold law using evaporatively cooled fermionic atoms. *Phys. Rev. Lett.*, 82:4208–4211, 1999.
- [21] C. Chin, R. Grimm, P. Julienne, and E. Tiesinga. Feshbach resonances in ultracold gases. *Rev. Mod. Phys.*, 82:1225–1286, 2010.
- [22] S. Wu, Y.-J. Wang, Q. Diot, and M. Prentiss. Splitting matter waves using an optimized standing-wave light-pulse sequence. *Phys. Rev. A*, 71:043602, 2005.
- [23] M. Edwards, B. Benton, J. Heward, and C. W. Clark. Momentum-space engineering of gaseous bose-einstein condensates. *Phys. Rev. A*, 82:063613, 2010.